



# Prediction of an EF4 supercell tornado in Funing, China: Resolution dependency of simulated tornadoes and their structures



Zhengqi Sun<sup>a</sup>, Ming Xue<sup>a,b,\*</sup>, Kefeng Zhu<sup>a</sup>, Bowen Zhou<sup>a</sup>

<sup>a</sup> Key Laboratory of Mesoscale Severe Weather/Ministry of Education, School of Atmospheric Sciences, Nanjing University, Nanjing, Jiangsu 210023, China

<sup>b</sup> Center for Analysis and Prediction of Storms and School of Meteorology, University of Oklahoma, Norman, OK 73072, USA

## ARTICLE INFO

### Keywords:

Tornado prediction  
Large eddy simulation  
Resolution dependency  
Multiple sub-vortices tornado

## ABSTRACT

An EF4 supercell tornado that occurred on 23 June 2016 in Funing, China is simulated using the WRF model. Five nested forecast experiments are run, with the horizontal grid spacing of the inner-most nest being 4000, 1333, 444, 148, and 49 m, respectively. All experiments reproduce the general characteristics of the observed supercell storm, but tornado-like vortex does not develop until the grid spacing is 444 m or less. The tornadoes on the 444, 148 and 49 m grids reach EF1, EF2 and EF3 intensities, respectively. The tornado vortex simulated on the 444 m grid tends to maintain a one-cell structure, while a ring of high-vorticity develops during the mature stage of the tornado vortex on the 148 m grid leading to a two-cell structure. On the 49 m grid, microscale vortices along the outflow boundary merge into and help organize the main tornado vortex while multiple ‘suction vortices’ develop later along the high-vorticity ring leading to a multi-vortex tornado. These sub-vortices create localized regions of intense winds due to the super-positioning of the sub-vortex and main vortex circulations and the system translation speed. Sub-vortices also create irregular strong surface wind patterns with localized ‘damage cores’, broadening the tornadic wind swath; these are consistent with the Funing tornado damage survey. Based on the results, we recommend a horizontal grid spacing of at least 500 m for real-time warn-on-forecast applications in order to capture tornado-like vortices while for tornado dynamics, prediction and predictability studies 50 m or less is recommended.

## 1. Introduction

For severe weather hazards and in particular tornadoes, [Stensrud et al. \(2009, 2013\)](#) discussed issuing warnings based on numerical weather prediction (NWP) model output rather than on observations, hence shifting the warning paradigm from warn-on-detection to warn-on-forecast. Recent forecast experiments have shown that forecast systems with horizontal grid spacings of 1 to 4 km can provide useful guidance for severe weather including tornadoes ([Loken et al., 2017](#); [Clark et al., 2018](#)). Certain diagnostic quantities, such as updraft helicity (UH) and low-level ( $\sim 1$  km above ground level or AGL) vertical vorticity ( $\xi$ ), have been used as surrogates to create probabilistic tornado forecasts from convection-allowing ensembles ([Clark et al., 2012](#); [Sobash et al., 2016a, 2016b](#)); however, convection-allowing models (CAMs) do not resolve tornadoes explicitly. Further, observational studies have suggested a weak relationship between mid-level rotation and tornado occurrence (e.g., [Trapp et al., 1999, 2005](#); [Markowski et al., 2011](#)). Specifically, [Trapp et al. \(2005\)](#) estimate that only 15% of storms with mid-level mesocyclones produce tornadoes. Therefore,

explicit simulations/predictions of tornado or tornado-scale circulations with high enough resolutions may be necessary for more reliable tornado forecasting.

Previous tornado-resolving simulations have mostly used idealized model configurations. [Lewellen et al. \(2000\)](#) conducted highly idealized large-eddy-resolving simulations of tornado and investigated the influence of swirl ratio on tornado intensification. [Rotunno et al. \(2016\)](#) produced axisymmetric tornado simulations and investigated the effects of turbulence in the boundary layer on a tornado vortex. More realistic simulations use a single sounding to define the storm environment and simulate tornadoes embedded within a parent storm (e.g., [Roberts et al., 2016](#); [Orf et al., 2017](#)). [Yao et al. \(2018\)](#) used a cloud model initialized from a sounding extracted from a real-data simulation to simulate tornadoes reaching EF4 in intensity for a case that occurred in northern Jiangsu Province of China, a case that is the subject of this study.

Tornadic structures are uncertain because of their small spatial scales, short lifetimes and complex wind fields. Although single-vortex tornadoes often occur, several smaller-scale sub-vortices can develop

\* Corresponding author at: CAPS, 120 David Boren Blvd, Norman, OK 73072, USA.

E-mail address: [mxue@ou.edu](mailto:mxue@ou.edu) (M. Xue).

within the primary vortex and revolve about its center (i.e., a multi-vortex tornado) (Agee et al., 1976; Rotunno, 1978). Idealized numerical studies using large eddy simulations (LESs) (e.g., Rotunno, 1984; Lewellen, 1993) produced vortices in the form of one-cell, two-cell and multi-vortex structures (Davies-Jones et al., 2001) and examined the structural features of these vortices. For a two-cell structure, a wall of updraft is located away from the tornado vortex center where a downdraft is found; multi-vortices often develop following the two-cell stage. Laboratory simulations (e.g., Church and Snow, 1993) obtained similar results.

Sub-vortices in multi-vortex tornadoes are referred to as ‘suction vortices’ in observational studies (e.g., Fujita, 1970), and have been documented in photographs, movies and video (e.g., Fujita, 1981), damage surveys and radar studies. Using Doppler-on-Wheels (DOW) mobile Doppler radars, Wurman (2002) was first to characterize the size, strength, motion, horizontal and vertical structure and persistence of multiple suction vortices in a tornado. The suction vortices are often associated with certain irregular tornado damage patterns called ‘suction marks’. Atkins et al. (2014) reported cusps and loops in the damage path of the 20 May 2013 EF5 Moore Oklahoma tornado. This damage pattern is believed to be due to multiple suction vortices rotating within the larger tornado vortex (Fujita et al., 1970), or associated with tornado(es) revolving around the larger-scale parent circulation, the low-level mesocyclone (Fujita, 1963; Agee et al., 1976; Brown and Knupp, 1980).

In comparison to observational studies, there are few studies that attempt to simulate real tornadoes from real initial conditions and investigate tornado vortex structures. Using a forecast at a horizontal grid spacing of 100 m, Schenkman et al. (2012) obtained successful simulations of a tornado-like-vortex (TLV) within a mesoscale convective system and investigated the tornadogenesis processes within. Xue et al. (2007, 2014) reproduced the 8 May 2003 Oklahoma City tornadic supercell. A tornado-strength vortex occurred at a location and time similar to observations on nested 100 m and 50 m grids; their 50 m simulation captured a two-cell tornado structure that had only previously been simulated using highly idealized setups. For the first time in a real data case, the 50 m simulation marginally resolved sub-vortices that developed along a ring of maximum vorticity. Detailed trajectory-based vorticity budget analyses on the simulation data suggest that vorticity generated by surface friction is an important source of vorticity in tornadogenesis (Schenkman et al., 2014). Most recently, Snook et al. (2019) reported on ensemble probabilistic forecasting of an EF5 intensity tornado at a 50 m grid spacing, employing ensemble Kalman filter data assimilation for initial conditions.

The above real case studies initialized forecasts via radar data assimilation. Mashiko et al. (2009) initialized forecasts at 50 m horizontal grid spacing from a mesoscale NWP model, but did not include radar data. The forecasts predicted the outer rainband of a landfalling typhoon, one storm spawned a tornado and its genesis process was analyzed in detail. Using a similar approach, Mashiko (2016) simulated a Tsukuba City supercell tornado and analyzed the vorticity sources of low- and mid-level mesocyclones. Mashiko and Niino (2017) recently simulated a multi-vortex tornado for the same supercell by nesting the forecast down to 10 m grid spacing. The case observed the evolution of a tornado from a one-cell to a two-cell vortex, followed by the development of multiple sub-vortices in the tornado. Vortex evolution was found to be closely related to the swirl ratio, as theory would predict.

Among the very limited number of real-case tornado simulations, none has focused on resolution dependency of tornado simulation/prediction. For supercell storms, Potvin and Flora (2015) found case-dependent sensitivity of idealized simulations to grid spacings ranging between 333 m and 4 km. Simulated updrafts and cold pools are sensitive to resolution; much of the sensitivity arises because small-scale processes are poorly resolved and in turn, impact the larger and better resolved scales. Based on simulations of squall lines at 1 km and 500, 250, and 125 m grid spacings, Bryan et al. (2003) suggested that 100 m

grid spacing or less is needed to accurately simulate deep moist convection. For explicit tornado simulations, Xue et al. (2007) suggested that a horizontal grid spacing at or below 50 m is needed although no detailed analysis was presented on resolution dependency.

In the afternoon of 23 June 2016, an EF4 tornado occurred in Funing County in northern Jiangsu Province, China. The tornado caused 99 human deaths and 846 injuries, and was the second EF4 tornado recorded in Jiangsu Province since 1950 (Xue et al., 2016; Zheng et al., 2016; Meng et al., 2018). In this study, the Funing tornado case is simulated using the advanced research version of the Weather Research and Forecasting (WRF-ARW) model (Skamarock et al., 2008) starting from a three-dimensional analysis of the NCEP operational Global Forecasting System (GFS). Different numbers of grid nesting levels are used in a set of five experiments, with the horizontal grid spacing of the innermost nest being 4 km, 1333 m, 444 m, 148 m, and 49 m, respectively. The resolution dependency and forecast implications are discussed in this paper in terms of simulated tornado structure, intensity and wind hazards. For the highest resolution grid (49 m grid spacing), the simulated tornado evolves from a one-cell, to a two-cell (with a horizontal vorticity ring) and finally to a multi-vortex stage. The impact of multiple ‘suction’ vortices on surface wind hazards within the simulation are discussed. Balancing the resolution requirements for explicitly simulating tornadoes and associated computational costs as well as forecast timeliness, the choices of resolution for numerical tornado prediction are suggested. Real-data, high-resolution simulations of tornadoes in China have not been reported in the formal literature before. The simulation data sets also provide a basis for future detailed diagnostic studies on tornado dynamics.

The rest of this paper is organized as follows. Section 2 provides a case overview of the Funing tornado case and Section 3 describes the design of numerical simulation experiments. Section 4 analyzes the structure and intensity of tornadic vortices simulated at different resolutions, in particular those simulated on the finest 49 m grid. A summary and conclusions are given in Section 5.

## 2. Case overview and environmental conditions

Funing County is located in northern Jiangsu Province in the Yangtze-Huaihe River Basin. The local terrain is mostly flat agricultural land (Fig. 1) and Jiangsu Province has the highest tornado occurrence frequency in China (Fan and Yu, 2015). The Funing tornado formed at approximately 0615 UTC (1415 LST) on 23 June 2016. It moved east-northeast at about 60 km per hour across Funing County and reached EF4 intensity at about 0620 UTC and again at 0635 UTC (Meng et al., 2018). The tornado dissipated at approximately 0700 UTC, although a weak and short-lived tornado formed about 10 min later further east in neighboring Sheyang County. The tornado produced a swath of EF1 – EF4 rated damage about 35 km long and up to 4.1 km wide (Meng et al., 2018). The mesoscale surface network captured a wide swath (25 km long, 10 km wide) of strong winds exceeding  $17.2 \text{ m s}^{-1}$ , with a recorded maximum wind speed of  $34.6 \text{ m s}^{-1}$  at 0629 UTC at the Funing Xingouzhen Station. The observed 1 h (0600–0700 UTC) accumulated precipitation was 56 mm at a nearby station. Due to heavy precipitation wrapping, no photograph of the tornado funnel was available, although videos of rotating air flows and flying debris were recorded (a video clip is provided as Supplemental material).

The tornado was spawned by a storm that developed south of a Meiyu frontal rainband, and the storm exhibited pronounced supercell characteristics after 0400 UTC. The low-level flows are southeasterly, setting up strong directional wind shear with the higher level winds being westerly. The supercell storm was about 30 km wide, the hook-shaped echo and strong cyclonic rotation were captured by the Yancheng S-band Doppler radar located about 80 km southeast the storm (Fig. 2g). More information on the development and evolution of the tornadic storm can be found in Xue et al. (2016); Meng et al. (2018) presents a detailed damage survey on this case.

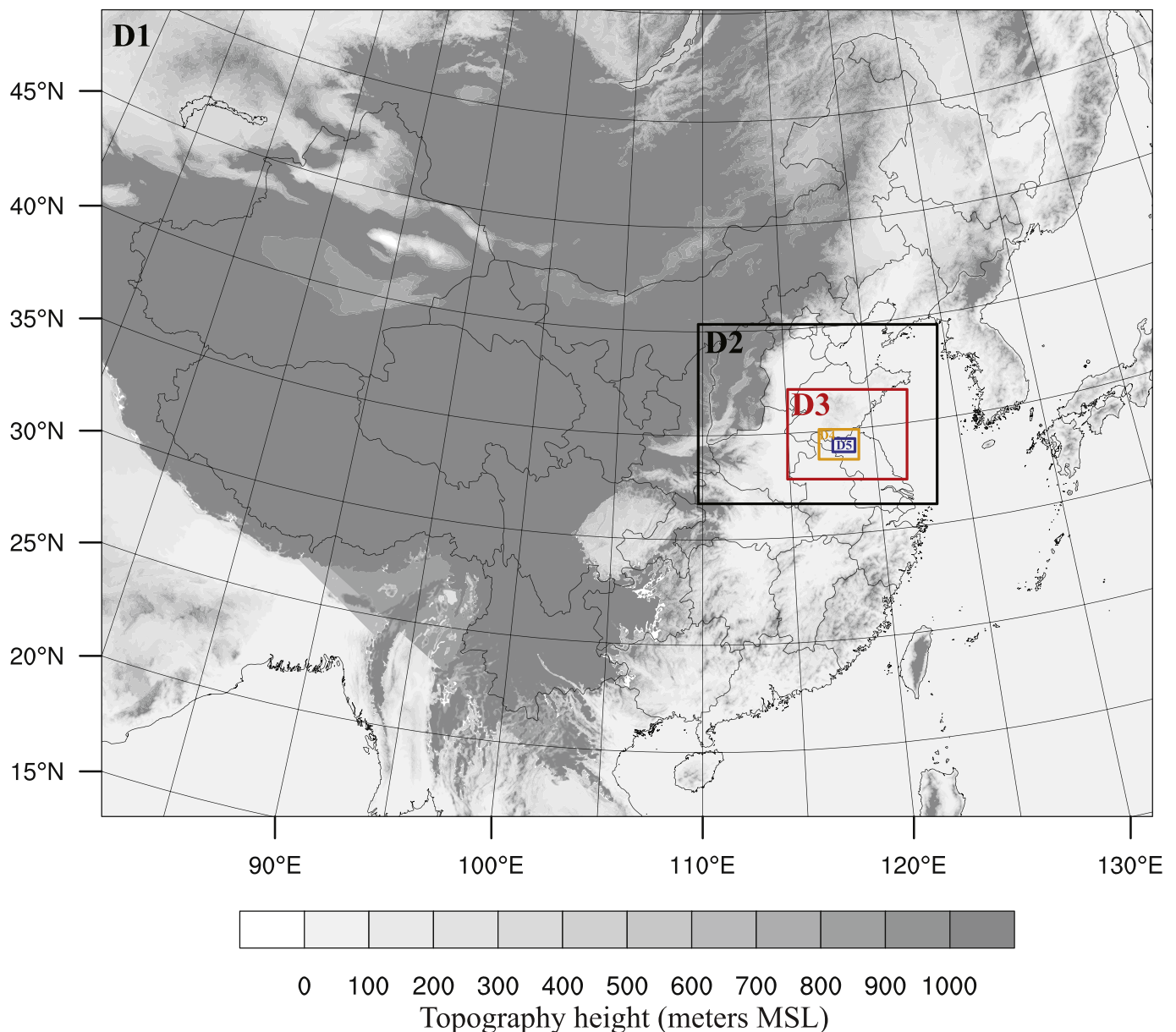


**Fig. 1.** The WRF simulation domains with terrain elevation. D1, D2, D3, D4 and D5 indicate the 5 levels of nested domains with horizontal grid spacings of 4 km, 1333 m, 444 m, 148 m, and 49 m, respectively.

At the time of the event, a quasi-stationary cold vortex was located in northeast China at 500 hPa (Fig. 3a). This synoptic weather pattern is often responsible for series of severe convective weather events in northern China during the summer. Funing (marked by the red star in Fig. 3) was located downstream of the 500 hPa trough; at the same time, an 850 hPa trough (blue line in Fig. 3b) extended from Shandong (SD in Fig. 3b) Province through the Sichuan (SC) Basin. The Western Pacific sub-tropical high ahead of the trough (Fig. 3b) advected warm moist air from the South China Sea to northern Anhui (AH) and Jiangsu (JS) provinces (Fig. 3b); the storm of interest first formed in northern Anhui and moved across northern Jiangsu (Xue et al., 2016).

The near-storm environmental conditions up to  $\sim 375$  hPa were captured by a sounding taken at 0600 UTC at Sheyang station, about 60 km east of the tornado location. The hodograph (Fig. 4a) shows 0–6 km layer wind shear was  $27.2 \text{ m s}^{-1}$ . Near the surface, the winds veered with height from east-southeasterly to southerly (Fig. 4a), creating strong shear in the lowest 1 km of the atmosphere ( $8.7 \text{ m s}^{-1} \text{ km}^{-1}$ ). At levels above 1 km height, wind shear was close to

unidirectional (Fig. 4a).

The 0600 UTC NCEP Operational GFS Final Analysis is used to fill the missing upper portion (above  $\sim 400$  hPa) of the observed sounding. A thin near-surface layer of humid, cold air in the sounding profile (Fig. 4b) appears to have been influenced by the outflow of precipitation (Fig. 4b) and is not believed to be representative of the southeasterly low-level inflow of the supercell storm. For this event, the maximum unstable convective available potential energy (MUCAPE) was  $2663 \text{ J kg}^{-1}$  and the convective inhibition (CIN) was  $8 \text{ J kg}^{-1}$ . Given the heavy precipitation associated with this event, the storm of interest was classified as a heavy precipitation (HP) type storm (Doswell III and Burgess, 1993). With a moderate-to-large CAPE and strong vertical wind shear, the environment was favorable for the formation of tornadic supercells (Moller et al., 1990).

### 3. Design of numerical experiments

The WRF-ARW model version 3.9 is used to simulate the 23 June

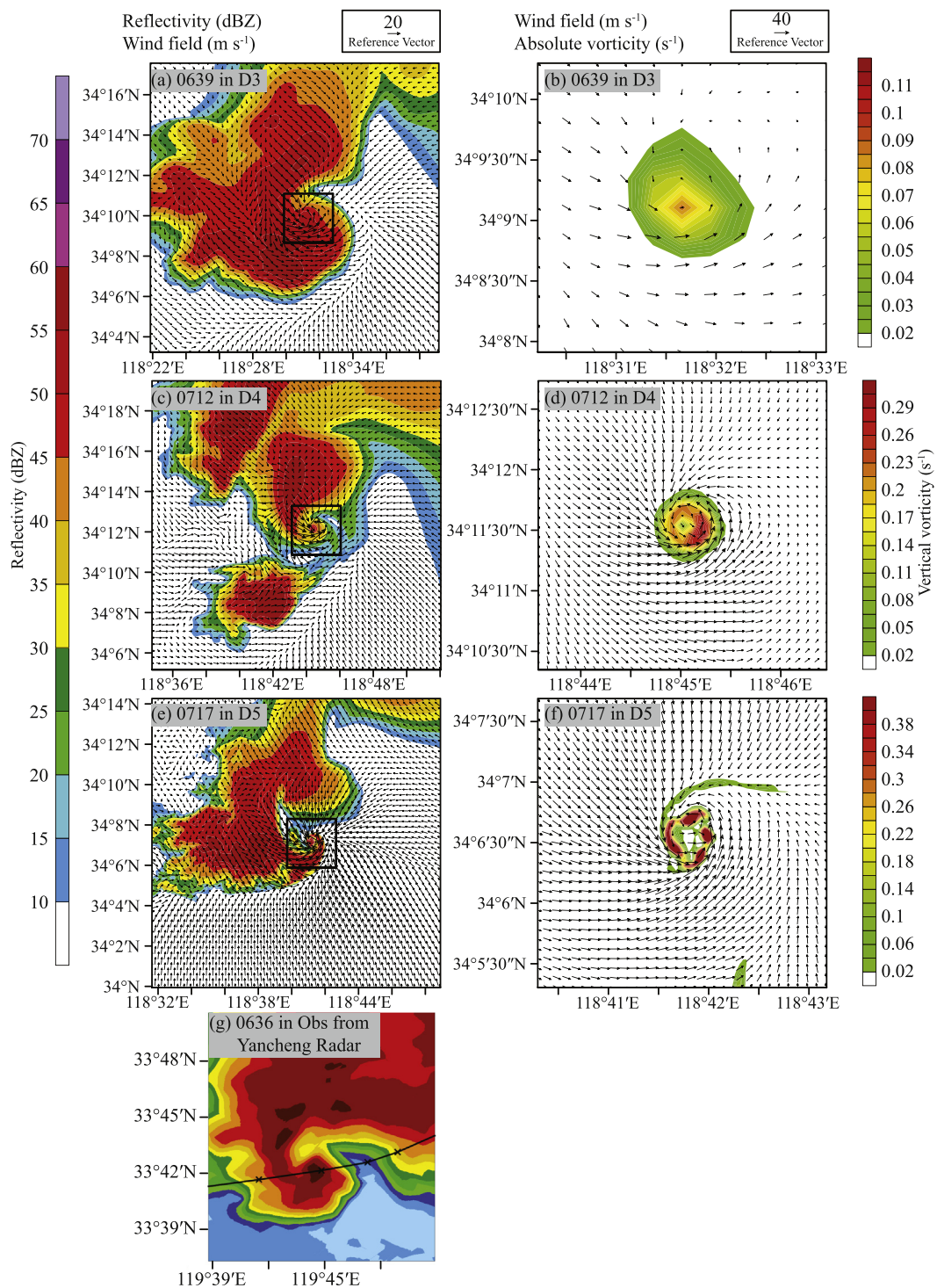
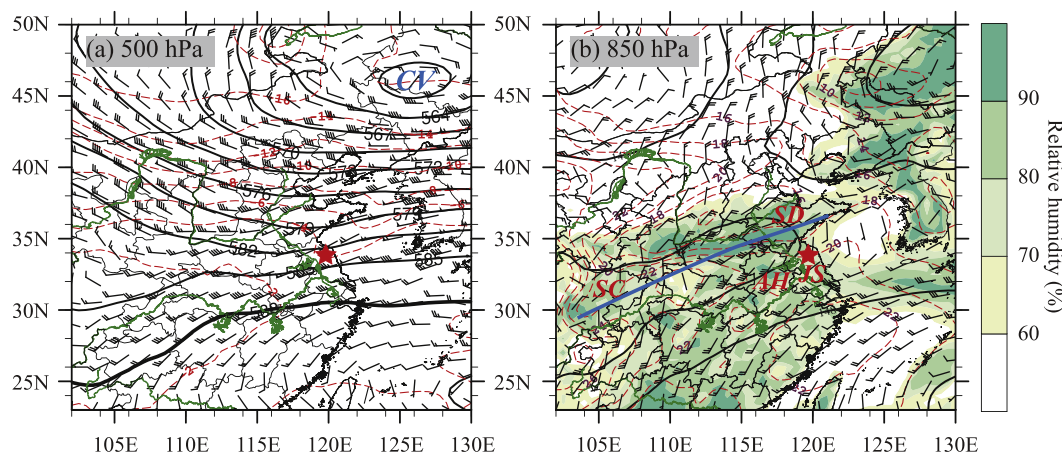


Fig. 2. (a)–(f) D3–D5 of D13–D15 simulated supercell reflectivity (left panels) and vertical vorticity (right panels) at the lowest model height above the surface (~26 m AGL). Horizontal wind vectors at the same height are included. Plots are taken at the time the tornado is mature. Black boxes in left-hand panels indicate the plotted domain for the corresponding right-hand panels. (g) Yancheng radar observed reflectivity (0.5° elevation angle).

2016 Funing EF4 tornado case using multiple levels of nested grids. The outer domain of the model spans continental China with 4-km horizontal grid spacing (Zhu et al., 2018). This forecast configuration was used to run real-time forecasts during the summer months at Nanjing University and exhibited a high level of skill at forecasting precipitation (Zhu et al., 2018). The forecast system also accurately reproduced the diurnal precipitation cycle for the Yangtze-Huaihe River Basin during the Meiyu season, the region and season this event occurred (Xue et al.,

2018; Zhang et al., 2019).

The 4-km domain has  $1409 \times 1081$  grid points in the horizontal. To study the resolution requirement and dependency of tornado simulation, 5 experiments are run with different number of grid nesting levels, with a 3:1 ratio between successive levels. With 1, 2, 3, 4 and 5 total number of nesting levels, the innermost grid of these experiments has a horizontal grid spacing of 4 km, 1333 m, 444 m, 148 m, and 49 m, respectively. The grids at the different levels are called grid D1 to D5,



**Fig. 3.** The NCEP operational GFS analysis of wind bars (a full bar is  $4\text{ m s}^{-1}$ ), geopotential height (black contour), and temperature (red contour) at (a) 500 hPa and (b) 850 hPa. Analyses are valid at 1200 UTC 1 June 2015. The cold vortex in (a) is marked as CV, relative humidity (shaded) is plotted in (b). A trough in (b) is marked with a dark blue line. Funing is marked by a red star, Shandong (SD), Anhui (AH), Jiangsu (JS) and Sichuan (SC) provinces are labeled. (For interpretation of the references to color in this figure legend, the reader is referred to the web version of this article.)

while the five experiments are referred to as D11, D12, D13, D14, and D15, respectively, with the numbers in the names indicating the range of grids included (Fig. 1). The outermost domain D1 is large enough to cover the entire Meiyu rainband while grids D4 and D5 contain the full length of simulated tornado path. Grid D5 is  $117\text{ km} \times 94\text{ km}$  and covers most of the observed tornado life cycle. All simulations have 51 vertical levels. The vertical grid is stretched with a minimum spacing of 26 m near the surface and 10 model levels reside within the lowest 1 km. The model top is at  $\sim 20\text{ km}$ .

D1 is initialized from the 23 June 2016 NCEP GFS 0000 UTC analysis and the GFS forecasts provide boundary conditions every 3 h. D2 and D3 are also initialized from the same GFS analysis. D4 and D5 are interpolated from their respective parent domain at 0435 and 0500 UTC, respectively. Detailed grid information and computational costs are listed in Table 1. Note that completing the simulation on the highest-resolution grid (D5) takes approximately 70 times more CPU core hours than the 4 km grid for the same number of grid points (every million number of horizontal grid points) and forecast duration.

All experiments use the 2-moment Morrison microphysics scheme, which predicts the number concentration and mixing ratio of four hydrometeor species including: cloud ice, rainwater, snow and graupel plus the mixing ratio for cloud water (Morrison and Grabowski, 2008).

The Pleim-Xiu land surface and surface layer models (Pleim, 2006) coupled with the Asymmetric Convective Model (Version 2, ACM2) PBL scheme (Pleim, 2007) are used. The Community Atmosphere Model (CAM3) radiation scheme is used to parameterize fluxes of long- and short-wave radiation (Collins et al., 2004). Grids D1 – D4 use the Smagorinsky deformation-based horizontal subgrid-scale (SGS) turbulence mixing parameterization (Smagorinsky, 1963), D5 uses the fully three-dimensional 1.5-order turbulent kinetic energy (TKE)-based SGS turbulence closure scheme based on Deardorff (1974). The TKE SGS closure scheme is appropriate for the 49 m grid given that it was originally designed and applied to LESs (Deardorff, 1974). None of the grids use cumulus parameterizations. Grids D1- D4 use the Smagorinsky horizontal turbulence scheme to avoid problems associated with using a prognostic TKE scheme in a two-way nested domain; when SGS TKE is calculated on different grids, the scheme samples different portions of the flow (Zhou et al., 2018). Except for the TKE scheme in D5, all other physics options are the same as those used in the real-time 4-km forecasting system (Zhu et al., 2018). An ensemble of forecasts on the same single 4-km grid (as in D11) using difference combination of physics parameterizations from the WRF model, following Zhu and Xue (2016), produced varying simulations of the tornadic storm, with the current configuration producing better results (not shown).

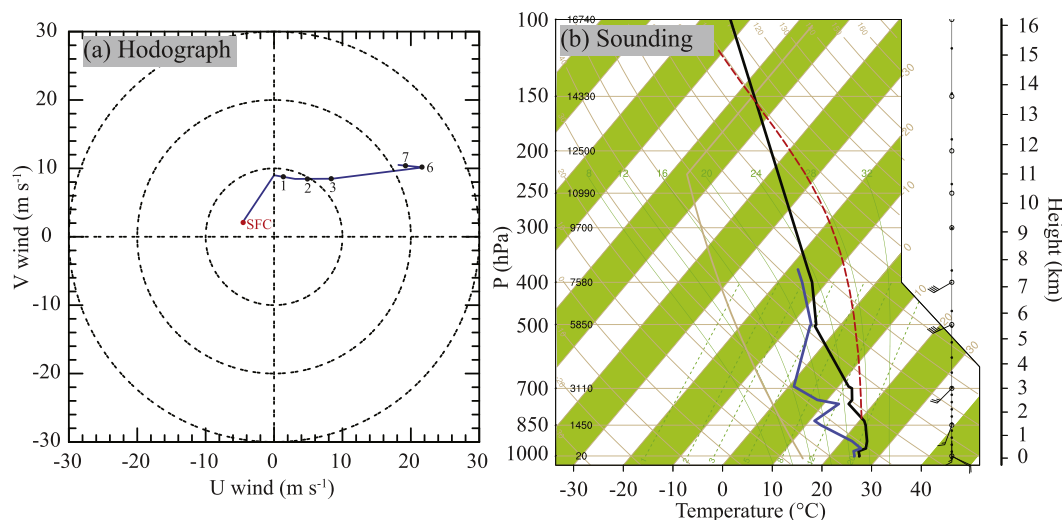


**Fig. 4.** The 06 UTC Sheyang Station sounding (a) hodograph and (b) T-ln(p). The station is about 60 km east of the Funing tornadic supercell storm. The observed sounding top is approximately 375 hPa, the upper portion is filled by the GFS analysis.

**Table 1**

Detailed model configuration and computation cost of each innermost domain of each experiment. Note that the computation time refers to real cost time for per million horizontal points, per simulation hour.

Domain	Grid number	Grid number	Time step (s)	Start time (UTC)	Computation time (960 Cores, per million horizontal grid points, per simulation hour)
D1	1408 × 1080	4	25	0000	0.03
D2	960 × 720	1.333	8.33	0000	0.09
D3	1440 × 1080	0.444	2.78	0000	0.2–0.3
D4	1440 × 1080	0.148	0.93	0435	0.7–0.8
D5	2400 × 1920	0.049	0.31	0500	2.0–2.1

Most previous real-case tornado simulation studies (Schenkman et al., 2012; Xue et al., 2014; Mashiko, 2016; Mashiko and Niino, 2017) used single-moment microphysics schemes, but this study uses the two-moment Morrison microphysics scheme (Morrison and Grabowski, 2008). Dawson et al. (2010, 2015) found that multi-moment microphysics schemes produced more realistic cold pools and simulated TLVs. The most recent tornado ensemble prediction study of Snook et al. (2019) also used a two-moment microphysics scheme. Land surface and radiation parameterization schemes are almost all column-based and do not consider horizontal fluxes. While three-dimensional radiative processes such as cloud anvil shading (e.g., Markowski and Harrington, 2005) may affect the simulated supercell storm, and certain three-dimensional radiation schemes (e.g., O'Hirok and Gautier, 1998) have been designed, such schemes are not available within the community WRF-ARW. The same column-based schemes are therefore used on all grids; the impact of model physics on the simulation of tornadic storms is a topic for future work.

## 4. Results and discussions

### 4.1. Genesis of tornado-like vortices

The general characteristics of the tornadic supercell, including the hook-shaped echo and rotating updrafts, are reproduced reasonably well in all five experiments. However, only experiments D13 through D15 are able to produce on their innermost nest tornado-like vortices (TLVs, Fig. 5). A TLV is a vortex where the maximum vertical vorticity  $\xi_{max}$  is very close to the ground surface (within 100 m or so) and is a product of near surface vortex intensification. Time-height plots of  $\xi_{max}$  show that on grid D2 of D12  $\xi_{max}$  occurs approximately 1 km AGL, this corresponds to a low-level mesocyclone (Fig. 5a) and does not qualify as a TLV. Large vertical vorticity values ( $\xi_{max} > 0.012 \text{ s}^{-1}$ ) associated with the mesocyclone descend towards the surface at 0640 UTC (Fig. 5a); however, surface vortex intensification does not occur. D12-predicted vertical velocity  $w$  values are relatively small ( $< 10 \text{ m s}^{-1}$ ) near the surface ( $< 900 \text{ m AGL}$ ) (Fig. 6a). A lack of intense, near-surface vertical acceleration limits stretching of the vertical vorticity, and hence no tornado vortex or TLV is explicitly predicted. Because D12 does not explicitly predict a TLV, one can only infer a high likelihood of a tornado occurrence, not the actual formation of a tornado.

Simulated vortices appear to be quite different when the grid spacing is decreased from 1.33 km (D2 of D12) to 444 m (D3 of D13). D13 predicts TLVs to form around 0540, 0630 and 0715 UTC (Fig. 5b). Throughout the forecast the near surface  $\xi$  is much larger than that of the mesocyclone located further aloft (Fig. 5b, note the differences in color tables used). At approximately 0540 UTC, the near surface TLV intensifies rapidly, and  $\xi_{max}$  increases from 0.04 to  $0.1 \text{ s}^{-1}$  within approximately 2 min.

Each of the TLV intensifications in D13 is preceded by strong updrafts descending towards the surface or intensify near the ground (Fig. 6b). A gradual lowering of the  $w = 10 \text{ m s}^{-1}$  contour from 1 km to 650 m occurs between 0500 and 0537 UTC, while the contour rapidly descends to 200 m AGL a few minutes after 0537 UTC. At 0545 UTC, the  $20 \text{ m s}^{-1}$   $w$  contour is 500 m AGL (Fig. 6b), this enhances the vertical acceleration of near-surface air parcels. Correspondingly, near

ground  $\xi$  reaches a maximum over the next few minutes, resulting in the first TLV (Fig. 5b). This TLV lasts for about 15 min and then weakens, the second and third TLVs form via similar processes at 0630 and 0715 UTC.

On the 148 m grid D4 of D14, the  $\xi_{max}$  plot (Fig. 5c) shows two more intense and persistent TLVs. From 0500 to 0540 UTC, the  $w = 10 \text{ m s}^{-1}$  contour descends steadily from  $\sim 1 \text{ km}$  to  $\sim 100 \text{ m AGL}$ , while the  $w = 20 \text{ m s}^{-1}$  contour descends steadily from  $\sim 2.5 \text{ km}$  to  $\sim 900 \text{ m AGL}$  over a similar time period. By 0537 UTC the updraft rapidly descends to  $\sim 250 \text{ m AGL}$  in about  $\sim 3 \text{ min}$  (Fig. 6c). Near surface  $\xi_{max}$  increases rapidly to above  $0.3 \text{ s}^{-1}$  within  $\sim 1 \text{ min}$ , corresponding to the genesis of TLV (Fig. 5c). The initial intensity of this TLV fluctuates; however, the TLV gains more strength at  $\sim 0608 \text{ UTC}$ , and maintains itself for 30 min. Around 0640 UTC, the TLV broadens (not shown) and weakens rapidly, the strong updraft ( $w > 20 \text{ m s}^{-1}$ ) dies out at the low levels and lifts to above 1.8 km AGL. The updraft re-intensifies after 0700 UTC;  $w$  exceeds  $30 \text{ m s}^{-1}$  at  $\sim 350 \text{ m AGL}$  by  $\sim 0710 \text{ UTC}$ ; the second TLV forms rapidly at similar time.

On the 49 m grid D5 of D15, strong updrafts descend towards the surface even more quickly.  $w$  exceeds  $30 \text{ m s}^{-1}$  at 600 m AGL at 0525 UTC, although the most intense near-surface vortex occurs at 0540 UTC (Fig. 5d). Compared to D14, D15 predicts  $\xi_{max}$  to be stronger but less persistent, exhibiting more fluctuations in intensity. At 0705 UTC, near-surface  $w$  increases dramatically ( $w > 50 \text{ m s}^{-1}$  at 500 m AGL) and  $\xi$  exceeds  $0.5 \text{ s}^{-1}$ . The large increase in intensity corresponds to the formation of multiple sub-vortices in the main tornado vortex; this will be discussed later (see Section 4.3). Given that sub-vortices are resolved by the 49 m grid, we should be able to call the near-surface vortices in D15 tornado vortices rather than TLVs. Since a TLV does not form in either D11 or D12, we will focus on D13, D14, and D15 for the rest of the study.

### 4.2. Tornado structure and intensity

D13 – D15 all successfully reproduce the supercell storm structure; the simulated hook echo (Fig. 2a, c, e) is similar to that of radar observed reflectivity (Fig. 2g). The simulated vortices strengthen with increased resolution from D3 to D5 (note the differences in color tables used), this is not apparent in the reflectivity fields. D3 (Fig. 2b) predicts a relatively broad vortex with a smooth  $\xi$  pattern, with  $\xi_{max}$  located on the south side of the vortex. D4 predicts the vortex to be tighter and more intense ( $\xi_{max} > 0.25 \text{ s}^{-1}$ ; Fig. 2d) than D3 ( $\xi_{max} > 0.07 \text{ s}^{-1}$ ; Fig. 2b), and  $\xi_{max}$  located on the southeastern edge of the vortex. The vortex exhibits a high-vorticity ring structure of a mature two-cell tornado (Fig. 2d).

The vortex predicted by D5 of D15 is distinct from the other experiments both in  $\xi$  patterns and flow structures (Fig. 2f). Four to five sub-vortices with local  $\xi$  maxima develop along the vorticity ring. As aforementioned, such sub-vortices correspond to observed 'suction vortices' in multi-vortex tornadoes and are known to cause extreme damage. In comparison, D3 and D4 resolve fewer details; both simulations lack detailed structure (Fig. 2b and d) and predict the TLVs to be of a single vortex or a vorticity ring structure, respectively.

Time series of instantaneous  $\xi_{max}$  at 10 m AGL, maximum horizontal wind speed  $V_{max}$  at 10 m AGL and minimum perturbation pressure  $p'_{min}$

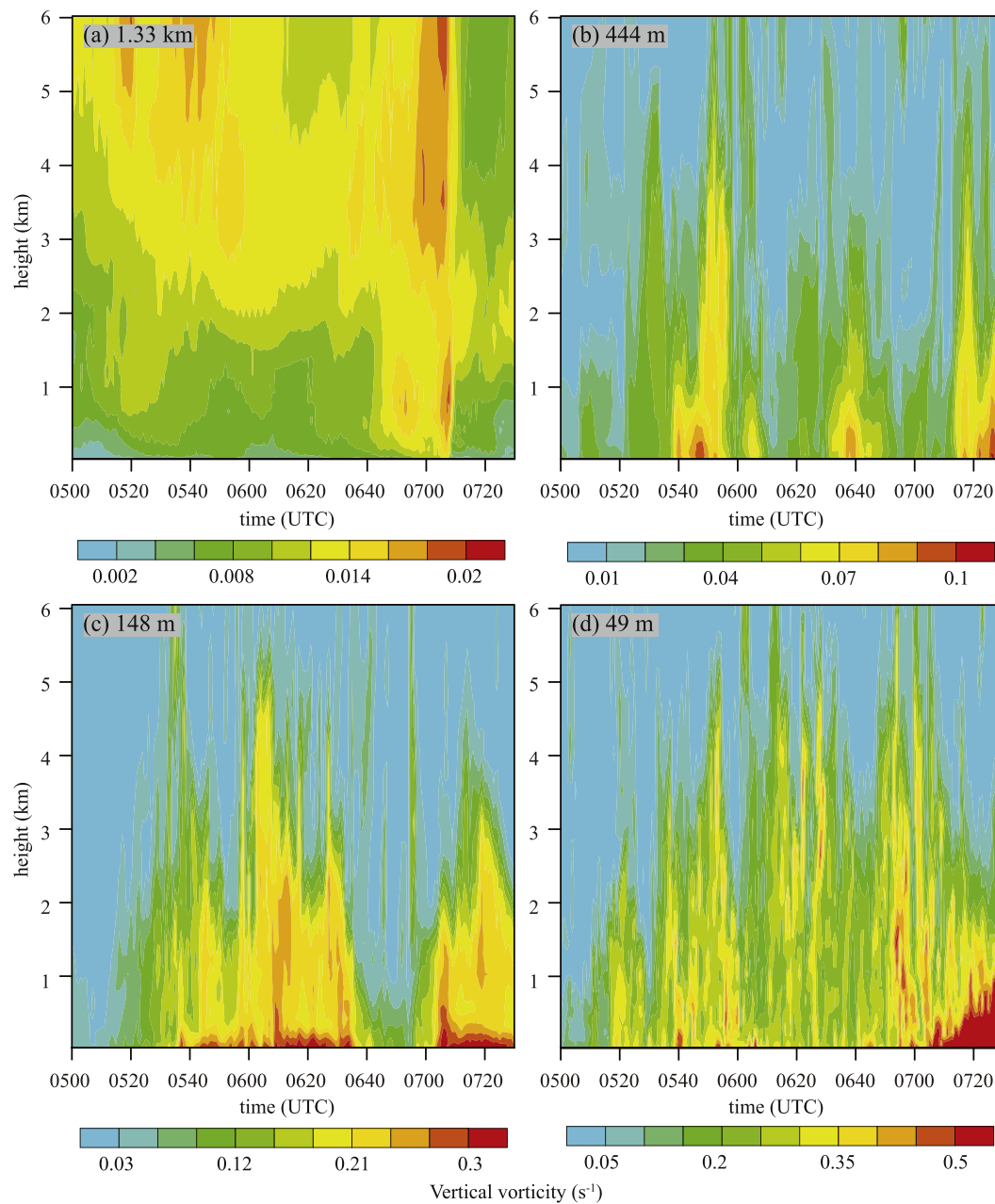


**Fig. 5.** Time-height plots of domain-wide  $\xi_{max}$  for grids (a) D2 of D12, (b) D3 of D13, (c) D4 of D14, and (d) D5 of D15, valid from 0500 to 0730 UTC. Data are output every minute. The color bars for vorticity are different for each subplot.

at the first model level above the surface ( $\sim 26$  m AGL) are plotted in Fig. 7. D3 of D13 predicts  $\xi_{max}$  to be  $< 0.1 \text{ s}^{-1}$  and to vary smoothly in time. Relatively large  $V_{max}$  ( $> 40 \text{ m s}^{-1}$ ) (Fig. 7b) and  $\xi_{max}$  values (Fig. 7a), and reduced  $p'_{min}$  ( $-14 \text{ hPa} - -10 \text{ hPa}$ ) (Fig. 7c) indicate that D3 predicts a near surface vortex to intensify to the maximum intensity of an EF1 tornado (Fig. 7b) on three separate occasions at 0550, 0640, and 0720 UTC. D4 of D14 predicts a dramatic increase in  $\xi_{max}$  ( $\sim 0.35 \text{ s}^{-1}$ ) (Fig. 7a) and  $V_{max}$  ( $> 50 \text{ m s}^{-1}$ ) (Fig. 7b) and a decrease in  $p'_{min}$  ( $-30 \text{ hPa}$ ) (Fig. 7c), the near surface vortex reaches EF2 intensity. During the simulation two TLVs occur at 0550–0635 UTC and 0705–0725 UTC; the second vortex is predicted to intensify more quickly than the first. It is noted that the damage survey of this case also noted periodic strengthening and weakening of the tornado vortex (Meng et al., 2018), though the simulation timing is somewhat off.

D5 of D15 simulates the strongest tornadic vortices, especially after 0700 UTC (Fig. 7). The experiment predicts  $\xi_{max}$  to exceed  $1.2 \text{ s}^{-1}$ , this

is an order of magnitude larger than D3 of D13, and more than three times that of D4 of D14. Similar to D3, there are three cycles of vortex intensification at 0530–0630, 0640–0655, and 0710–0730 UTC, respectively. D5 predicts  $V_{max}$ ,  $\xi_{max}$ , and  $p'_{min}$  to be slightly larger than D4 until the final vortex intensification at 0710 UTC, when  $\xi$  becomes much larger and  $V_{max}$  exceeds  $65 \text{ m s}^{-1}$  at 10 m AGL (EF3 intensity) (Fig. 7b) and  $p'_{min}$  drops  $> 50 \text{ hPa}$  (Fig. 7c). The rapid increase in  $\xi_{max}$ ,  $V_{max}$  and  $|p'_{min}|$  is accompanied by the development of small intense sub-vortices within the tornado vortex, as will be discussed more later. The sub-vortices are only resolved in D5, this is similar to the results of high-resolution tornado simulations in Xue et al. (2014).

#### 4.3. Structure and evolution of simulated tornado vortices on the 49 m grid

In this section, we examine the simulated tornado vortex structure and evolution on the 49 m grid in more detail, in particular the

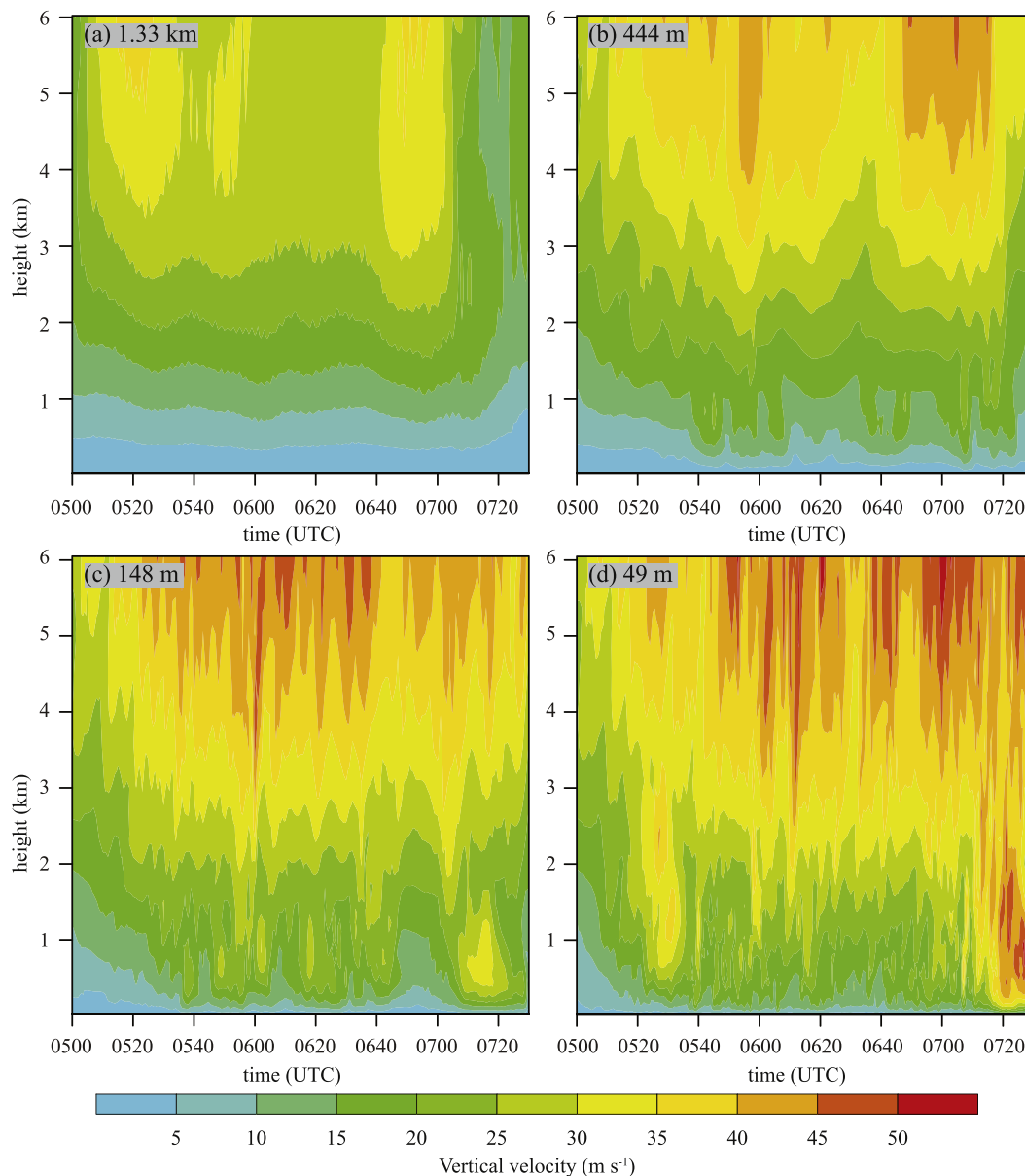


Fig. 6. Time-height plots of domain-wide maximum  $w$  for grids (a) D2 of D12, (b) D3 of D13, (c) D4 of D14, and (d) D5 of D15, valid from 0500 to 0730 UTC. Data are output every minute.

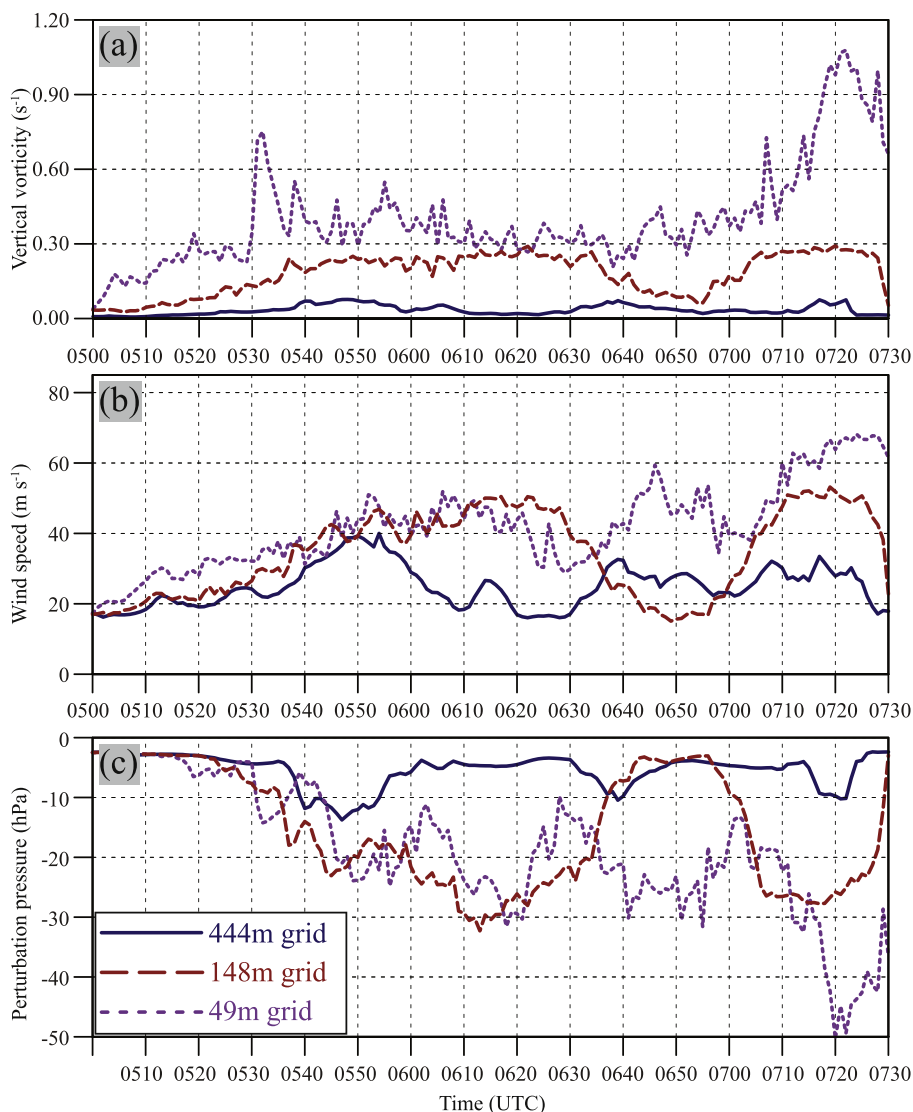
evolution of the main tornado vortex from a one-cell to two-cell and finally a multi-vortex tornado.

Fig. 8 shows the horizontal and vertical cross sections of velocity and  $\xi$  fields associated with the simulated tornado on D5 at 0655, 0716 and 0724 UTC, the times when low-level  $\xi$  starts to increase rapidly, reaches about half of the peak intensity, and reaches the peak intensity, respectively (Fig. 7a). The strength of the main tornado vortex changes rapidly during this period. At 0655 UTC, the tornado has a well-defined ‘one-cell’ (Davies-Jones et al., 2001) structure (Fig. 8a). A west-east vertical cross section through the vortex core (Fig. 8b) shows an updraft located in the center of a single-vortex, downdrafts are located on the vortex edge in the lowest km of the atmosphere. Another local maximum in  $\xi$  is located about 1.5 to 2.0 km AGL, which suggests the spiral ascent of large vertical vorticity values in the tornado vortex.

The structure and organization of the tornado vortex evolve rapidly during intensification (0655–0716 UTC). The one-cell vortex structure observed at 0655 UTC (Fig. 8a) evolves into a ‘vorticity ring’ structure by 0700 UTC (Fig. 9a), where the largest  $\xi$  is concentrated in a ring displaced from the vortex center. A series of small vortices (labeled V1 –

V5 in Fig. 9a) develop along a band of increased  $\xi$  north of the tornado vortex at 0655 UTC (Fig. 8a). From 0700 to 0706 UTC these small vortices revolve counter-clockwise around the main tornado vortex and are drawn into the vortex by a strong near-surface convergent flow (Fig. 9a – g). By 0704 UTC, vortices V1 – V3 are absorbed by the main vortex, which shrinks in size to re-establish a concentrated one-cell structure (Fig. 9e). Over a period of two minutes (0704–0706 UTC), the one-cell structure evolves into the ring vortex structure (Fig. 9h) as vortices V4 – V6 are absorbed into the main vortex.

The tornado vortex organizes into a well-defined ring structure by 0716 UTC (Fig. 8c) with increased  $\xi_{max}$  (Fig. 7a). While the vorticity ring is mostly circular at this time, undulations in the flow suggest 4 to 5 waves are developing (Fig. 8c). A pronounced “two-cell” (Davies-Jones et al., 2001) structure is evident in the corresponding cross-section (Fig. 8d). Large  $\xi$  is displaced from the vortex center and large positive  $w$  is found outside the ring (Fig. 8c) where radial flow convergence is strongest. A downdraft ( $|w| > 16 \text{ m s}^{-1}$ ) extends from approximately 0–2 km AGL within the vorticity ring. On the east side of the vortex, a strong ( $w \sim 26 \text{ m s}^{-1}$ ) low-level (400 m AGL) updraft



**Fig. 7.** (blue) D3, (red) D4, and (purple) D5 predicted maximum near-surface (10 m AGL) (a) vertical vorticity, (b) wind speed, and (c) first model level ( $\sim 26$  m AGL) minimum perturbation pressure from 0500 to 0730 UTC. Data are output every minute. (For interpretation of the references to color in this figure legend, the reader is referred to the web version of this article.)

induces intense vertical stretching of  $\xi$ . The vertical structure of the tornado vortex vorticity ring is analogous to the eye wall of a mature hurricane, a comparison that has been previously drawn in observational studies of intense tornadoes (e.g., Lee and Wurman, 2005).

Between 0716 and 0724 UTC, 5 sub-vortices with distinct  $\xi$  maxima develop along the vorticity ring (Fig. 8e) and  $\xi_{max}$  almost doubles (Fig. 7a).  $p'_{min}$  decreases to  $\sim -50$  hPa (Fig. 7c); pressure perturbations are lowest at the center of the small sub-vortices due to centrifugal effects. Large near-surface wind speeds ( $V_{max} > 65 \text{ m s}^{-1}$ ) (Fig. 7b) occur because the circulation of the sub-vortices is superimposed onto the main tornado vortex circulation. The sub-vortices are relatively shallow and are vertically tilted (Fig. 8f). It is noted that the vortex on the eastern side of the cross-section is stronger above the ground but tilts outside the vertical plane at  $\sim 250$  m AGL. Sub-vortices are generally as deep as the original vortex ring in Fig. 8d ( $\sim 700$  m AGL).

Within the sub-vortices (e.g., the one at  $x = 37$  in Fig. 8f), enhanced positive and negative  $w$  coexist. Strong downdrafts are induced by a downward pressure gradient force and an updraft promoting vortex intensification. Previous studies suggest multiple sub-vortices form along the vorticity ring because barotropic instability (Rotunno, 1978; Lee and Wurman, 2005) promotes vortex Rossby waves. This process is

commonly discussed in the tropical cyclone community (Montgomery and Kallenbach, 1997; Möller and Montgomery, 1999). The repeated evolution of a tornado (one-cell, two-cell and multi-vortex) was also documented in a recent supercell simulation (Mashiko and Niino, 2017).

Surface winds and vertical vorticity are analyzed at the one-cell (Fig. 10a) and multiple-vortex (Fig. 10b) tornado stages. At the one-cell stage (0655 UTC) (Fig. 10a, corresponding to Fig. 8a), the vortex circulation is generally circular. The parent supercell storm has an eastward movement speed of about  $12 \text{ m s}^{-1}$ , and the tornado vortex tangential wind speed is about  $33 \text{ m s}^{-1}$ , giving rise to maximum ground relative wind speed of over  $45 \text{ m s}^{-1}$  on the south side of the main tornado vortex (Fig. 10a). By 0724 UTC, five sub-vortices with distinct  $\xi$  maxima are found within the main tornado vortex (Fig. 10b). Again, the main tornado vortex wind speed on the south (north) side of the vortex is larger (smaller) due to the addition (subtraction) of the main vortex circulation and translation speed. On the south and southwest side of the main vortex the maximum wind speed exceeds  $68 \text{ m s}^{-1}$ , in the south and southwest part of the two sub-vortices, respectively, the circulations of two sub-vortices further enhance near surface winds (Fig. 10b). Cores of extreme wind speeds are only 50–100 m (1 to 2 grid

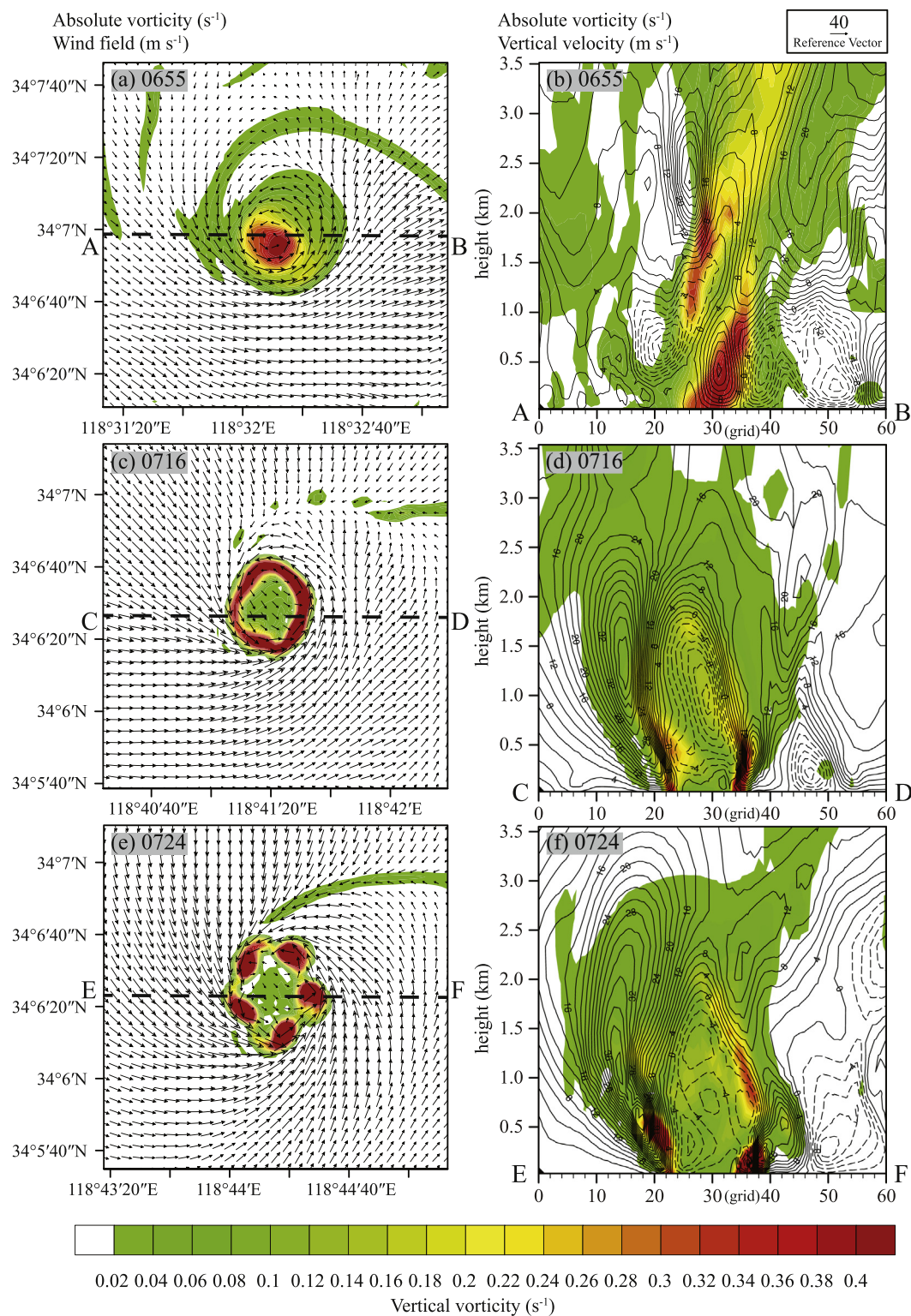


**Fig. 8.** (a, c, e) Horizontal cross sections of D5 predicted vertical vorticity and horizontal wind vectors at  $\sim 26$  m AGL. (b, d, f) Vertical cross sections of vertical vorticity and vertical velocity (contours every  $2\text{ m s}^{-1}$  with negative contours dashed). The location of the cross-sections is marked as a dashed line in (a, c, e). The plotted times are shown in the figure.

intervals) in size, and can cause extremely localized, intense damages.

#### 4.4. Simulated ground-level vorticity and wind swaths

Beside maximum intensity, the tornado path length and wind hazard coverage are of great concern in tornado forecasts (Dahl et al.,

2017). D13, D14 and D15 predicted maximum swaths of near-surface  $\xi$  and wind speed are analyzed between 0500 and 0730 UTC (Fig. 11). Swaths are indicative of tornado damage. Forecast maximum swaths demonstrate the gradual weakening and strengthening of the low-level vortex (Fig. 11).  $\xi_{max}$  is located near the main vortex center in D3 of D13 (Fig. 11a) and D4 of D14 (Fig. 11c). Both simulations predict a

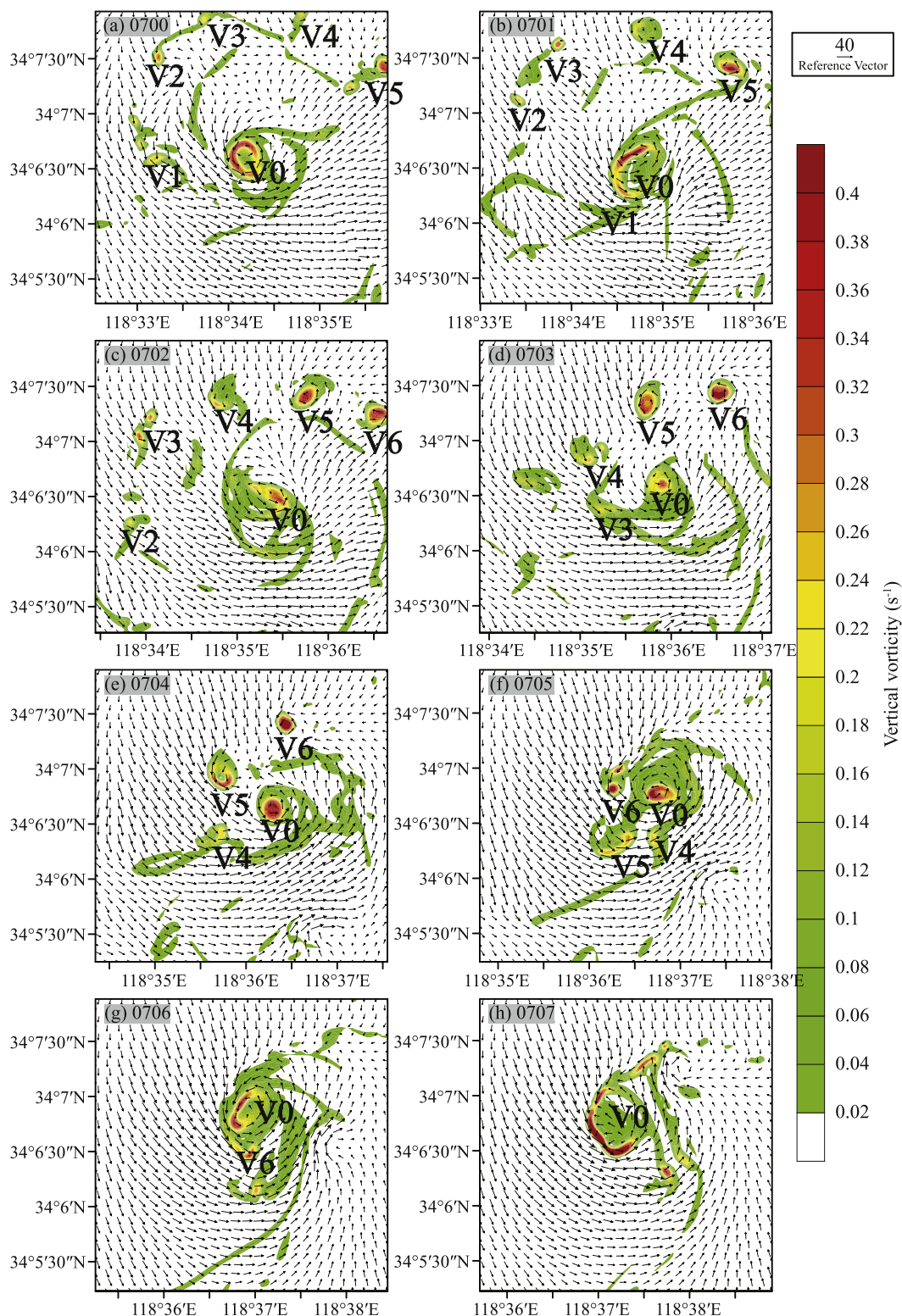


**Fig. 9.** Horizontal cross sections of D5 predicted vertical vorticity and horizontal wind vectors at the first model level (26 m AGL) at (a) 0700, (b) 0701, (c) 0702, (d) 0703, (e) 0704, (f) 0705, (g) 0706, and (h) 0707 UTC. The main tornado vortex is marked “V0”, sub-vortices revolving around the main vortex are marked “V1”–“V6”.

relatively smooth and straight tornado path (Fig. 11a, c) as well as strong surface winds (Fig. 11b, d). D5 of D15 predicts multiple sub-tracks of high wind speed that revolve around the central vortex and swing over the main ‘damage track’ (Fig. 11f). This phenomenon occurs during all three periods of vortex intensification, and is most

pronounced during the third period after 0700 UTC (inside the black rectangle in Fig. 11e, f and Fig. 12). Sub-tracks of strong wind are associated with the small vortices that form around and are eventually drawn into the main vortex in the earlier stages (as shown in Fig. 9). Later in the simulation they are produced by the intense sub-vortices

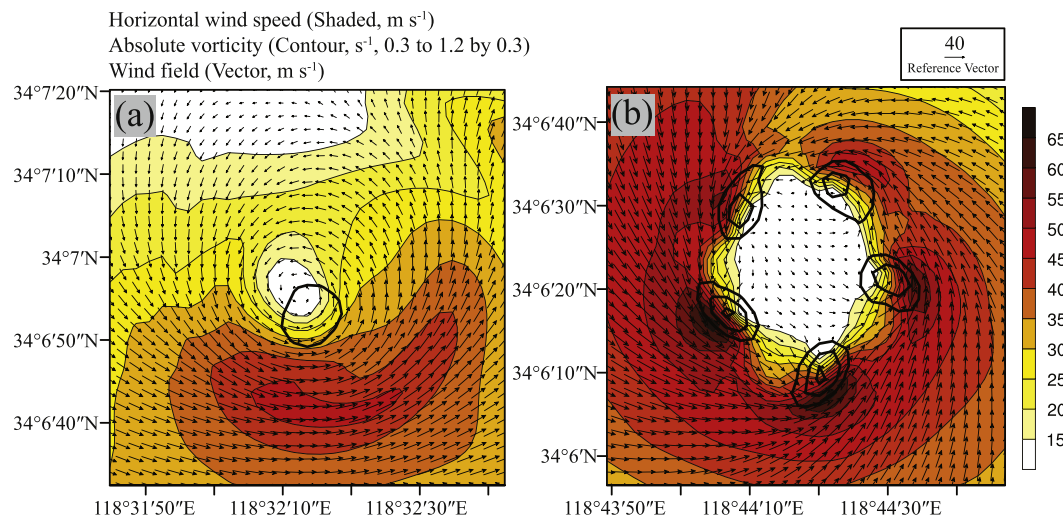


**Fig. 10.** Horizontal cross section of D5 predicted horizontal wind speed, vertical vorticity (thick contours,  $s^{-1}$ ), and horizontal wind vectors at 10 m AGL. Plots examine the vortex at (a) 0655 and (b) 0724 UTC.

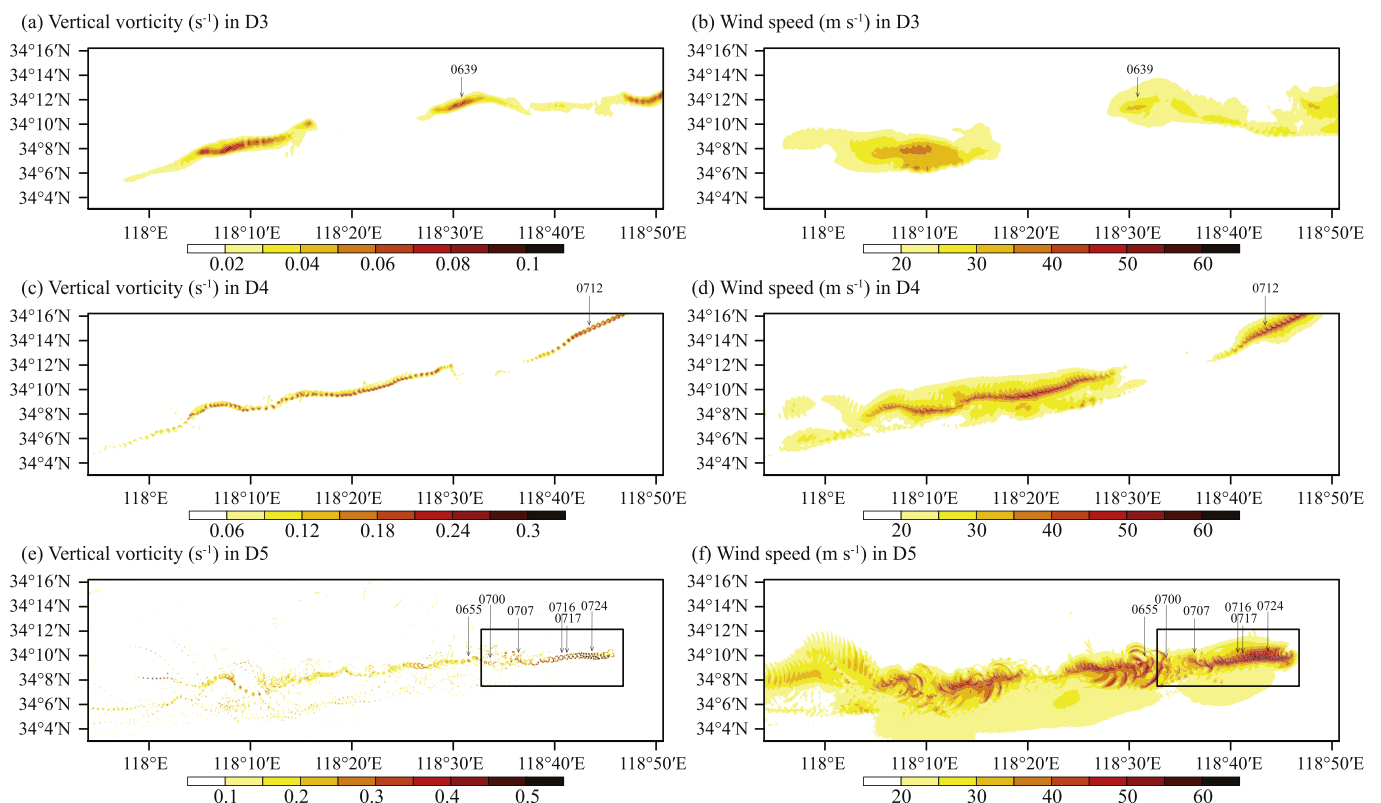


**Fig. 11.** (a, b) D3 of D13, (c, d) D4 of D14 and (e, f) D5 of D15 forecast maximum swaths of vertical vorticity (left panels) and wind speed (right panels) at 10 m AGL. Swaths are of simulated tornadic vortices and are indicative of the tornado damage paths. Model output frequency is every minute from 0500 to 0730 UTC. Vertical arrows denote the time occurrence of a predicted feature. Black boxes in (e) and (f) marker the subdomain plotted in Fig. 12.

(i.e., suction vortices) that develop within the main tornado vortex (Fig. 8e).

D15 (Fig. 11f) predicts the tornado to produce a swath of strong surface winds that is wider than both D13 and D14 predictions (Fig. 11b, d) and causes more widespread wind hazards. D15 predicts the swath of wind speed exceeding  $50\text{ m s}^{-1}$  to be as wide as 4 km ( $118^{\circ}30'E$ , Fig. 11f). Wide swaths of damage with irregular, sporadic, and intense ‘damage cores’ (Fig. 12) are consistent with the tornado damage report (Meng et al., 2018). In comparison, D13 and D14 are run at too coarse resolutions (444 m and 148 m horizontal grid spacing,

respectively) to simulate this level of realism.

Despite the large differences in the simulated vortex and wind structures, the overall tornado damage paths in experiments D13, D14 and D15 extend over a similar region (Fig. 11). Each experiment predicts the main tornado vortex to go through 2 to 3 cycles of intensification and decay (Fig. 7) and at certain point the strongest surface wind falls below the minimum of EF0 tornado threshold (e.g., in D13, Fig. 11b) and the tornadoes on ground become distinct ones. While each simulation produces multiple tornadoes, the tornadoes are all produced by the same mesocyclone (not shown) and the persistence

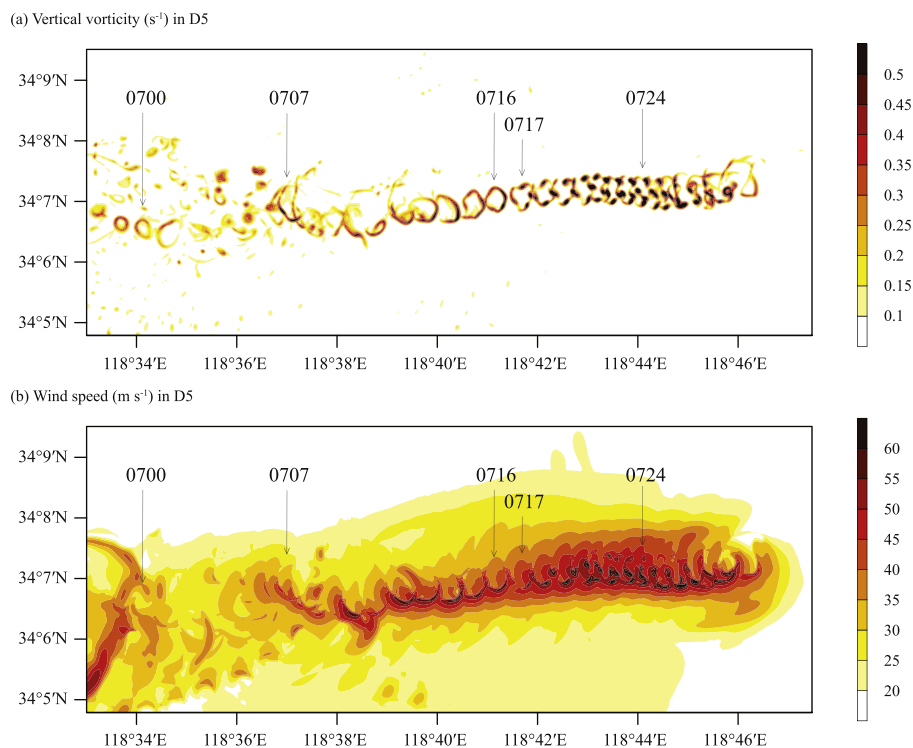


**Fig. 12.** Swaths of D5 forecast maximum (a) vertical vorticity and (b) wind speed at 10 m AGL. Rectangles in Fig. 11 e and f, denote the domain plotted in (a) and (b), respectively. Model output frequency is every minute from 0700 to 0730 UTC.

of the tornado vortex does not seem to monotonically depend on the resolution.

Despite timing differences, the consistency between the simulated tornadoes or TLVs in D13 – D15 in terms of the overall vortex structure suggests a good degree of tornado predictability when the parent supercell storm and mesocyclone are skillfully predicted. A distinct structural improvement is obtained when the horizontal resolution is extended into the LES regime (i.e., from 144 m to 49 m in this study). LESs resolve more fine-scale details such as micro-scale sub-vortices associated with the cold pool gust fronts, cold surge boundaries, and the sub-vortices developing within the main tornado vortex. Explicitly forecasting the microscale vortices is of a practical importance because it leads to structural differences in the predicted tornado and significantly impacts the intensity and distribution of surface wind hazards (Dahl et al., 2017).

The results of our resolution dependency study are generally consistent with previous real-case supercell tornado simulations (Xue et al., 2014; Mashiko and Niino, 2017) and with other simulation studies of different types of tornadoes (e.g., Rotunno and Klemp, 1985; Mashiko et al., 2009; Schenkman et al., 2011a, 2011b). Results are also consistent with the scale of the physical features to be resolved. This study is the first real-data tornado-resolving modeling study of a tornado in China.

## 5. Summary and conclusions

This real-data study uses the WRF-ARW model to simulate a supercell and embedded tornadoes, for a case that produced an EF4 tornado in eastern China. One to five, two-way-interactive nested model domains are used to run forecasts at innermost horizontal grid spacings ranging from 4 km to 49 m. The operational NCEP GFS analysis and forecasts provide the initial and boundary conditions for outermost domain.

The general characteristics of the supercell are reasonably captured by the forecasts, even for the experiment that uses a single 4 km grid. A

tornado-like vortex does not develop until a horizontal grid spacing of at least 444 m is used and this forecast predicts the maximum surface 10-m wind to reach EF1 intensity. Vortex intensity in terms of both near surface wind speed and vorticity increases with resolution, reaching EF2 and EF3 intensities on the 148 and 49 m grids, respectively. The forecast on the 49 m grid predicts microscale vortices to form along the outflow boundary and merge and organize into the main tornado vortex. Multiple ‘suction vortices’ that develop along the high-vorticity ring within the main tornado vortex are explicitly resolved at this resolution. The simulated ‘suction vortices’ are relatively shallow and vertically tilted, these vortices are approximately the same depth as the strong vorticity ring ( $< 700$  m AGL).

Due to superposition of storm translation velocity, tangential velocity of the main tornado vortex, and tangential velocity of the sub-vortices, the strongest surface wind speeds are found in the south and southwest part of the two sub-vortices. The presence of multiple microscale vortices create irregular, arc-shaped wind damage paths (i.e., suction marks) that cause intense damage cores. Additionally, strong surface winds cause more widespread wind hazards. The irregular, wide damage path with localized ‘damage cores’ is consistent with the Funing tornado damage survey (Meng et al., 2018). Only the forecast run on the 49 m grid is able to resolve the multi-vortices.

Our results suggest that horizontal grid spacings smaller than  $\sim 500$  m are necessary to simulate and predict tornado-like vortices in supercell storms while grid spacings close to 50 m are needed to capture sub-tornado-vortex-scale structures such as multi-vortices that cause localized, intense damage. Coarser resolutions under-estimate surface maximum wind speed. Forecasts run at horizontal grid spacings of 1.33 and 4 km can only capture strong rotating updrafts and large updraft helicity indicative of strong tornado potential (not shown), not tornado-like vortices with near-surface vorticity maxima.

To simulate the tornado on a 50 km by 50 km domain (which is generally small for a real-simulation) at  $\sim 50$  m grid spacing using 960 computing cores takes approximately two hours of wall clock time for a one hour simulation. For real-time warn-on-forecast applications, at

least an order of magnitude increase in computational speed is needed to run timely forecasts. Balancing the trade-off between explicitly forecasting tornadic vortices and damage intensity and computational expense, we recommend real-time tornado forecasts be run at horizontal grid spacings of at least 500 m to be able to resolve tornado-like vortices; however, forecasts need to be run at ~50 m horizontal grid spacing for research studies on tornado dynamics, prediction and predictability.

This study is based on simulations of a single case that occurred in China; however, the supercell of this case is typical of a HP supercell, with environmental CAPE and shear typical of those of supercells also. Further, the results of this study are consistent with previous tornado simulation studies. For these reasons, we believe our conclusions on resolution dependency of simulated supercell tornadoes have general applicability. Still, additional studies are needed to further test the generality of the conclusions, and for other types of tornadoes also. Smaller and/or weaker non-supercell tornadoes may require higher resolution forecasts than relatively large supercell tornadoes.

Finally, we point out this is the first successful simulation of real tornado in China that is initialized from a three-dimensional analysis, and is the first study to focus on the resolution requirement for simulating real tornadoes. To our knowledge, this is also the first time the widely used community WRF model has been used to simulate tornadoes at a tornado-resolving resolution.

Supplementary data to this article can be found online at <https://doi.org/10.1016/j.atmosres.2019.06.019>.

## Acknowledgments

This work was primarily supported by NSFC grant 41730965 and NJCAR grant NJCAR2016ZD02. The second author was also supported by VORTEX-SE grant NA17OAR4590188. Jon Labriola is thanked for proofreading the final manuscript.

## References

- Agee, E.M., Snow, J.T., Clare, P.R., 1976. Multiple vortex features in the tornado cyclone and the occurrence of tornado families. *Mon. Weather Rev.* 104, 552–563. [https://doi.org/10.1175/1520-0493\(1976\)104<0552:mvfitt>2.0.co;2](https://doi.org/10.1175/1520-0493(1976)104<0552:mvfitt>2.0.co;2).
- Atkins, N.T., Butler, K.M., Flynn, K.R., Wakimoto, R.M., 2014. An integrated damage, visual, and radar analysis of the 2013 Moore, Oklahoma, EF5 Tornado. *Bull. Amer. Meteor. Soc.* 95, 1549–1561. <https://doi.org/10.1175/Bams-D-14-00033.1>.
- Brown, J.M., Knupp, K.R., 1980. The Iowa cyclonic-anticyclonic tornado pair and its parent thunderstorm. *Mon. Weather Rev.* 108, 1626–1646. [https://doi.org/10.1175/1520-0493\(1980\)108<1626:ticatp>2.0.co;2](https://doi.org/10.1175/1520-0493(1980)108<1626:ticatp>2.0.co;2).
- Bryan, G.H., Wyngaard, J.C., Fritsch, J.M., 2003. Resolution requirements for the simulation of deep moist convection. *Mon. Weather Rev.* 131, 2394–2416. [https://doi.org/10.1175/1520-0493\(2003\)131<2394:Rrftso>2.0.co;2](https://doi.org/10.1175/1520-0493(2003)131<2394:Rrftso>2.0.co;2).
- Church, C.R., Snow, J.T., 1993. Laboratory models of tornadoes. In: *Geophys. Monogr.*, No.79, Amer. Geophys. Union, pp. 277–295. <https://doi.org/10.1029/GM079p0277>.
- Clark, A.J., Kain, J.S., Marsh, P.T., Correia, J., Xue, M., Kong, F.Y., 2012. Forecasting tornado pathlengths using a three-dimensional object identification algorithm applied to convection-allowing forecasts. *Weather Forecast.* 27, 1090–1113. <https://doi.org/10.1175/Waf-D-11-00147.1>.
- Clark, A.J., Jirak, I.L., Dembek, S.R., Creager, G.J., Kong, F.Y., Thomas, K.W., Knopfmeier, K.H., Gallo, B.T., Melick, C.J., Xue, M., Brewster, K.A., Jung, Y.S., Kennedy, A., Dong, X.Q., Markel, J., Gilmore, M., Romine, G.S., Fossell, K.R., Sobash, R.A., Carley, J.R., Ferrier, B.S., Pyle, M., Alexander, C.R., Weiss, S.J., Kain, J.S., Wicker, L.J., Thompson, G., Adams-Selin, R.D., Imy, D.A., 2018. The community leveraged unified ensemble (Clue) in the 2016 NOAA/hazardous weather testbed spring forecasting experiment. *Bull. Amer. Meteor. Soc.* 99, 1433–1448. <https://doi.org/10.1175/Bams-D-16-0309.1>.
- Collins, W.D., Rasch, P.J., Boville, B.A., Hack, J.J., Mccaa, J.R., Williamson, D.L., Kiehl, J.T., Briegleb, B., Bitz, C., Lin, S.-J., Zhang, M., Dai, Y., 2004. Description of the NCAR Community Atmosphere Model (CAM 3.0). NCAR Technical Note NCAR/TN-464 + STR. National Center for Atmospheric Research, Boulder, CO, pp. 226. <https://doi.org/10.5065/D63N21CH>.
- Dahl, N.A., Nolan, D.S., Bryan, G.H., Rotunno, R., 2017. Using high-resolution simulations to quantify underestimates of tornado intensity from in situ observations. *Mon. Weather Rev.* 145, 1963–1982. <https://doi.org/10.1175/Mwr-D-16-0346.1>.
- Davies-Jones, R., Trapp, R.J., Bluestein, H.B., 2001. Tornadoes and tornadic storms. In: *Meteor. Monogr.*, No.50, Amer. Meteor. Soc, pp. 167–222. <https://doi.org/10.1175/0065-9401-28.50.167>.
- Dawson, D.T., Xue, M., Milbrandt, J.A., Yau, M.K., 2010. Comparison of evaporation and cold pool development between single-moment and multimoment bulk microphysics schemes in idealized simulations of tornadic thunderstorms. *Mon. Weather Rev.* 138, 1152–1171. <https://doi.org/10.1175/2009mwr2956.1>.
- Dawson, D.T., Xue, M., Milbrandt, J.A., Shapiro, A., 2015. Sensitivity of real-data simulations of the 3 May 1999 Oklahoma City tornadic supercell and associated tornadoes to multimoment microphysics. Part I: storm- and tornado-scale numerical forecasts. *Mon. Weather Rev.* 143, 2241–2265. <https://doi.org/10.1175/mwr-d-14-00279.1>.
- Deardorff, J.W., 1974. Three-dimensional numerical study of turbulence in an entraining mixed layer. *Bound. Layer Meteor.* 7, 199–226. <https://doi.org/10.1007/bf00227913>.
- Doswell III, C.A., Burgess, D.W., 1993. Tornadoes and tornadic storms: a review of conceptual models. In: *Geophys. Monogr.*, No.79, Amer. Geophys. Union, pp. 75–88. <https://doi.org/10.1029/GM079p0161>.
- Fan, W., Yu, X., 2015. Characteristics of spatial-temporal distribution of tornadoes in China. *Meteorology* 41, 793–805 (in Chinese).
- Fujita, T.T., 1963. Analytical Mesometeorology. A Review. Severe local storms, No.5. American Meteorological Society, pp. 77–125. <https://doi.org/10.1007/978-1-940033-56-3.5>.
- Fujita, T.T., 1970. The Lubbock tornadoes: a study of suction spots. *Weatherwise* 23, 160–173. <https://doi.org/10.1080/00431672.1970.9932888>.
- Fujita, T.T., 1981. Tornadoes and downbursts in the context of generalized planetary scales. *J. Atmos. Sci.* 38, 1511–1534. [https://doi.org/10.1175/1520-0469\(1981\)038<1511:Taditc>2.0.Co;2](https://doi.org/10.1175/1520-0469(1981)038<1511:Taditc>2.0.Co;2).
- Fujita, T.T., Bradbury, D.L., Vanthull, C.F., 1970. palm sunday tornadoes of April 11, 1965. *Mon. Weather Rev.* 98, 29. [https://doi.org/10.1175/1520-0493\(1970\)098<0029:Pstoa>2.3.Co;2](https://doi.org/10.1175/1520-0493(1970)098<0029:Pstoa>2.3.Co;2).
- Lee, W.C., Wurman, J., 2005. Diagnosed three-dimensional axisymmetric structure of the Mulhall Tornado on 3 May 1999. *J. Atmos. Sci.* 62, 2373–2393. <https://doi.org/10.1175/Jas3489.1>.
- Lewellen, W.S., 1993. Tornado Vortex Theory. *Geophys. Monogr.*, No.79, Amer. Geophys. Union, pp. 19–39. <https://doi.org/10.1029/GM079p0019>.
- Lewellen, D.C., Lewellen, W.S., Xia, J., 2000. The influence of a local swirl ratio on tornado intensification near the surface. *J. Atmos. Sci.* 57, 527–544. [https://doi.org/10.1175/1520-0469\(2000\)057<0527:Tioals>2.0.Co;2](https://doi.org/10.1175/1520-0469(2000)057<0527:Tioals>2.0.Co;2).
- Loken, E.D., Clark, A.J., Xue, M., Kong, F., 2017. Comparison of next-day probabilistic severe weather forecasts from coarse- and fine-resolution CAMs and a convection-allowing ensemble. *Weather Forecast.* 32, 1403–1421. <https://doi.org/10.1175/waf-d-16-0200.1>.
- Markowski, P.M., Harrington, J.Y., 2005. A simulation of a supercell thunderstorm with emulated radiative cooling beneath the anvil. *J. Atmos. Sci.* 62, 2607–2617. <https://doi.org/10.1175/JAS3497.1>.
- Markowski, P.M., Majcen, M., Richardson, Y., Marquis, J., Wurman, J., 2011. Characteristics of the wind field in three nontornadic low-level mesocyclones observed by the doppler on wheels radars. *Electron. J. Sev. Storms Meteor.* 6, 1–48.
- Mashiko, W., 2016. A numerical study of the 6 May 2012 Tsukuba City supercell tornado. Part I: vorticity sources of low-level and midlevel mesocyclones. *Mon. Weather Rev.* 144, 1069–1092. <https://doi.org/10.1175/Mwr-D-15-0123.1>.
- Mashiko, W., Niino, H., 2017. Super high-resolution simulation of the 6 May 2012 Tsukuba supercell tornado: near-surface structure and its evolution. *Sola* 13, 135–139. <https://doi.org/10.2151/sola.2017-025>.
- Mashiko, W., Niino, H., Kato, T., 2009. Numerical simulation of tornadogenesis in an outer-rainband minisupercell of typhoon shanshan on 17 September 2006. *Mon. Weather Rev.* 137, 4238–4260. <https://doi.org/10.1175/2009MWR2959.1>.
- Meng, Z., Bai, L., Zhang, M., Wu, Z., Li, Z., Pu, M., Zheng, Y., Wang, X., Yao, D., Xue, M., Zhao, K., Li, Z., Peng, S., Li, L., 2018. The deadliest tornado (EF4) in the past 40 years in China. *Weather Forecast.* 33, 693–713. <https://doi.org/10.1175/waf-d-17-0085.1>.
- Möller, J.D., Montgomery, M.T., 1999. Vortex rosbay waves and hurricane intensification in a barotropic model. *J. Atmos. Sci.* 56, 1674–1687. <https://doi.org/10.1175/1520-04699902819999929056<1674%3avrwhi>2.0.co%3b2>.
- Moller, A.R., Doswell III, C.A., Przybylinski, R., 1990. High precipitation supercells: A conceptual model and documentation. Preprints. In: 16th Conf. On Severe Local Storms, Amer. Meteor. Soc., Kananaskis Park, AB, Canada, pp. 52–57.
- Montgomery, M.T., Kallenbach, R.J., 1997. A theory for vortex Rossby-waves and its application to spiral bands and intensity changes in hurricanes. *Q. J. R. Meteorol. Soc.* 123, 435–465. <https://doi.org/10.1256/Smsqj.53809>.
- Morrison, H., Grabowski, W.W., 2008. A novel approach for representing ice microphysics in models: description and tests using a kinematic framework. *J. Atmos. Sci.* 65, 1528–1548. <https://doi.org/10.1175/2007jas2491.1>.
- O'Hirok, W., Gautier, C., 1998. A three-dimensional radiative transfer model to investigate the solar radiation within a cloudy atmosphere. Part I: spatial effects. *J. Atmos. Sci.* 55, 2162–2179. [https://doi.org/10.1175/1520-0469\(1998\)055<2162:Atdrtm>2.0.Co;2](https://doi.org/10.1175/1520-0469(1998)055<2162:Atdrtm>2.0.Co;2).
- Orf, L., Wilhelmson, R., Lee, B., Finley, C., Houston, A., 2017. Evolution of a long-track violent tornado within a simulated supercell. *Bull. Amer. Meteor. Soc.* 98, 45–68. <https://doi.org/10.1175/bams-d-15-00073.1>.
- Pleim, J.E., 2006. A simple, efficient solution of flux-profile relationships in the atmospheric surface layer. *J. Appl. Meteor. Climatol.* 45, 341–347. <https://doi.org/10.1175/Jam2339.1>.
- Pleim, J.E., 2007. A combined local and nonlocal closure model for the atmospheric boundary layer. Part I: model description and testing. *J. Appl. Meteor. Climatol.* 46, 1383–1395. <https://doi.org/10.1175/Jam2539.1>.
- Potvin, C.K., Flora, M.L., 2015. Sensitivity of idealized supercell simulations to horizontal grid spacing: implications for warn-on-forecast. *Mon. Weather Rev.* 143, 2998–3024. <https://doi.org/10.1175/Mwr-D-14-00416.1>.
- Roberts, B., Xue, M., Schenkman, A.D., Dawson, D.T., 2016. The role of surface drag in tornadogenesis within an idealized supercell simulation. *J. Atmos. Sci.* 73, 3371–3395. <https://doi.org/10.1175/jas-d-15-0332.1>.

- Rotunno, R., 1978. A note on the stability of a cylindrical vortex sheet. *J. Fluid Mech.* 87, 761. <https://doi.org/10.1017/s0022112078001871>.
- Rotunno, R., 1984. An investigation of a three-dimensional asymmetric vortex. *J. Atmos. Sci.* 41, 283–298. [https://doi.org/10.1175/1520-0469\(1984\)041<0283:aiotad>2.0.co;2](https://doi.org/10.1175/1520-0469(1984)041<0283:aiotad>2.0.co;2).
- Rotunno, R., Klemp, J., 1985. On the rotation and propagation of simulated supercell thunderstorms. *J. Atmos. Sci.* 42, 271–292. [https://doi.org/10.1175/1520-0469\(1985\)042<0271:Otrapo>2.0.Co;2](https://doi.org/10.1175/1520-0469(1985)042<0271:Otrapo>2.0.Co;2).
- Rotunno, R., Bryan, G.H., Nolan, D.S., Dahl, N.A., 2016. Axisymmetric tornado simulations at high Reynolds number. *J. Atmos. Sci.* 73, 3843–3854. <https://doi.org/10.1175/Jas-D-16-0038.1>.
- Schenkman, A.D., Xue, M., Shapiro, A., Brewster, K., Gao, J.D., 2011a. Impact of CASA radar and Oklahoma Mesonet data assimilation on the analysis and prediction of tornadic mesovortices in an MCS. *Mon. Weather Rev.* 139, 3422–3445. <https://doi.org/10.1175/Mwr-D-10-05051.1>.
- Schenkman, A.D., Xue, M., Shapiro, A., Brewster, K., Gao, J.D., 2011b. The analysis and prediction of the 8–9 May 2007 Oklahoma tornadic mesoscale convective system by assimilating WSR-88D and CASA radar data using 3DVAR. *Mon. Weather Rev.* 139, 224–246. <https://doi.org/10.1175/2010MWR3336.1>.
- Schenkman, A.D., Xue, M., Shapiro, A., 2012. Tornadogenesis in a simulated mesovortex within a mesoscale convective system. *J. Atmos. Sci.* 69, 3372–3390. <https://doi.org/10.1175/Jas-D-12-038.1>.
- Schenkman, A.D., Xue, M., Hu, M., 2014. Tornadogenesis in a high-resolution simulation of the 8 May 2003 Oklahoma City supercell. *J. Atmos. Sci.* 71, 130–154. <https://doi.org/10.1175/Jas-D-13-073.1>.
- Skamarock, W.C., Klemp, J.B., Dudhia, J., Gill, D.O., Barker, D.M., Duda, M.G., Huang, X.-Y., Wang, W., Powers, J.G., 2008. A Description of the Advanced Research WRF Version 3. NCAR Technical Note NCAR/TN-475 + STR. National Center for Atmospheric Research, Boulder, CO, pp. 113.
- Smagorinsky, J., 1963. General circulation experiments with the primitive equations. *Mon. Weather Rev.* 91, 99–164. [https://doi.org/10.1175/1520-0493\(1963\)091<0099:gcewtp>2.3.co;2](https://doi.org/10.1175/1520-0493(1963)091<0099:gcewtp>2.3.co;2).
- Snook, N., Xue, M., Jung, Y., 2019. Tornado-resolving ensemble and probabilistic predictions of the 20 May 2013 Newcastle–Moore EF5 Tornado. *Mon. Weather Rev.* 147, 1215–1235. <https://doi.org/10.1175/mwr-d-18-0236.1>.
- Sobash, R.A., Romine, G.S., Schwartz II, C.S., Gagne, D.J., Weisman, M.L., 2016a. Explicit forecasts of low-level rotation from convection-allowing models for next-day tornado prediction. *Weather Forecast.* 31, 1591–1614. <https://doi.org/10.1175/waf-d-16-0073.1>.
- Sobash, R.A., Schwartz, C.S., Romine, G.S., Fossell, K.R., Weisman, M.L., 2016b. Severe weather prediction using storm surrogates from an ensemble forecasting system. *Weather Forecast.* 31, 255–271. <https://doi.org/10.1175/waf-d-15-0138.1>.
- Stensrud, D.J., Xue, M., Wicker, L.J., Kelleher, K.E., Foster, M.P., Schaefer, J.T., Schneider, R.S., Benjamin, S.G., Weygandt, S.S., Ferree, J.T., Tuell, J.P., 2009. Convective-scale warn-on-forecast system a vision for 2020. *Bull. Amer. Meteor. Soc.* 90, 1487. <https://doi.org/10.1175/2009BAMS2795.1>.
- Stensrud, D.J., Wicker, L.J., Xue, M., Dawson, D.T., Yussouf, N., Wheatley, D.M., Thompson, T.E., Snook, N.A., Smith, T.M., Schenkman, A.D., Potvin, C.K., Mansell, E.R., Lei, T., Kuhlman, K.M., Jung, Y., Jones, T.A., Gao, J.D., Coniglio, M.C., Brooks, H.E., Brewster, K.A., 2013. Progress and challenges with warn-on-forecast. *Atmos. Res.* 123, 2–16. <https://doi.org/10.1016/j.atmosres.2012.04.004>.
- Trapp, R.J., Mitchell, E.D., Tipton, G.A., Effertz, D.W., Watson, A.I., Andra, D.L., Magsig, M.A., 1999. Descending and nondescending tornadic vortex signatures detected by WSR-88Ds. *Weather Forecast.* 14, 625–639. [https://doi.org/10.1175/1520-0434\(1999\)014<0625:dantvs>2.0.co;2](https://doi.org/10.1175/1520-0434(1999)014<0625:dantvs>2.0.co;2).
- Trapp, R.J., Stumpf, G.J., Manross, K.L., 2005. A reassessment of the percentage of tornadic mesocyclones. *Weather Forecast.* 20, 680–687. <https://doi.org/10.1175/Waf864.1>.
- Wurman, J., 2002. The multiple-vortex structure of a Tornado. *Weather Forecast.* 17, 473–505. [https://doi.org/10.1175/1520-0434\(2002\)017<0473:tmvsoa>2.0.co;2](https://doi.org/10.1175/1520-0434(2002)017<0473:tmvsoa>2.0.co;2).
- Xue, M., Droegeleier, K.K., Weber, D., 2007. Numerical prediction of high-impact local weather: a driver for petascale computing. In: *Petascale Computing: Algorithms and Applications*. Taylor & Francis Group, LLC, pp. 103–124 (doi:10.1.1.74.2247).
- Xue, M., Hu, M., Schenkman, A.D., 2014. Numerical prediction of the 8 May 2003 Oklahoma City tornadic supercell and embedded tornado using ARPS with the assimilation of WSR-88D data. *Weather Forecast.* 29, 39–62. <https://doi.org/10.1175/waf-d-13-00029.1>.
- Xue, M., Zhao, K., Wang, M.J., Li, Z.H., Zheng, Y.G., 2016. Recent significant tornadoes in China. *Adv. Atmos. Sci.* 33, 1209–1217. <https://doi.org/10.1007/s00376-016-6005-2>.
- Xue, M., Luo, X., Zhu, K.F., Sun, Z.Q., Fei, J.F., 2018. The controlling role of boundary layer inertial oscillations in Meiyu frontal precipitation and its diurnal cycles over China. *J. Geophys. Res.* 123, 5090–5115. <https://doi.org/10.1029/2018JD028368>.
- Yao, D., Xue, H.L., Yin, J.F., Sun, J.S., Liang, X.D., Guo, J.P., 2018. Investigation into the formation, structure, and evolution of an EF4 tornado in East China using a high-resolution numerical simulation. *J. Meteor. Res.* 32, 157–171. <https://doi.org/10.1007/s13351-018-7083-0>.
- Zhang, Y., Xue, M., Zhu, K., Zhou, B., 2019. What is the main cause of diurnal variation and nocturnal peak of summer precipitation in Sichuan Basin, China? The key role of boundary layer low-level jet inertial oscillations. *J. Geophys. Res.* 124, 2643–2664. <https://doi.org/10.1029/2018jd029834>.
- Zheng, Y., Xue, M., Li, B., Chen, J., Tao, Z., 2016. Spatial characteristics of extreme rainfall over China with hourly through 24-hour accumulation periods based on national-level hourly rain gauge data. *Adv. Atmos. Sci.* 33, 1218–1232. <https://doi.org/10.1007/s00376-016-6128-5>.
- Zhou, B., Xue, M., Zhu, K., 2018. A grid-refinement-based approach to modeling the convective boundary layer in the gray zone: Algorithm Implementation and Testing. *J. Atmos. Sci.* 75, 1143–1161. <https://doi.org/10.1175/JAS-D-16-0376.1>.
- Zhu, K., Xue, M., 2016. Evaluation of WRF-based convection-permitting multi-physics ensemble forecasts over China for an extreme rainfall event on 21 July 2012 in Beijing. *Adv. Atmos. Sci.* 33, 1240–1258. <https://doi.org/10.1007/s00376-016-6202-z>.
- Zhu, K.F., Xue, M., Zhou, B.W., Zhao, K., Sun, Z.Q., Fu, P.L., Zheng, Y.G., Zhang, X.L., Meng, Q.T., 2018. Evaluation of real-time convection-permitting precipitation forecasts in China during the 2013–2014 summer season. *J. Geophys. Res.* 123, 1037–1064. <https://doi.org/10.1002/2017JD027445>.